ATOM INTERFEROMETRY

Edited by

Paul R. Berman

PHYSICS DEPARTMENT
UNIVERSITY OF MICHIGAN
ANN ARBOR, MICHIGAN

ACADEMIC PRESS 1997

San Diego London Boston
New York Sydney Tokyo Toronto

Contents

GENERALIZED TALBOT–LAU ATOM INTERFEROMETRY

JOHN F. CLAUSER AND SHIFANG LI
Department of Physics, University of California—Berkeley

I. Introduction

More than 20 years ago, Altshuler and Frantz (1973), with great foresight, proposed the possibility of directly observing the de Broglie wave spatial interference exhibited by the propagation of whole neutral atoms. More recently, the idea of building an atom interferometer again was proposed independently by Dubetskii *et al.*, (1984), Chebotayev and coworkers (1985), and Clauser (1988, 1989, 1991). Soon thereafter, a wide variety of atom interferometer configurations was demonstrated. Among these are what are commonly called *grating interferometers*. In a solid grating interferometer, coherent path separation is accomplished by passing atom de Broglie waves through carefully tailored aperture sets (e.g., slits) in a solid membrane, while in a "light grating" interferometer a standing-wave phase grating replaces the solid amplitude grating.

This chapter describes a particular form of grating interferometer that we have developed, called the *generalized Talbot–Lau* (GTL) interferometer. In Sections II and III, we first identify a significant weakness (low throughput) of

ISBN 0-12-092460-9

its progenitor form, separated beam envelope (SBE) interferometry, outline the operating principles of GTL interferometry, and show how GTL interferometry remedies this weakness. GTL interferometry is based on a unique form of interference, intimately associated with Fresnel diffraction, that occurs when Fraunhofer diffraction orders overlap. This effect was originally discovered in the optical domain using lenses and gratings and is called the *Talbot effect*. Its diffraction pattern consists of so-called Fourier and Fresnel fringes that, surprisingly, are actually multiply "aliased" near self-images of a grating's periodic complex amplitude transmission function. In Sections IV and V, we introduce the Talbot effect and give a brief historical outline of work contributing to its understanding. Sections VI and VII summarize its surprising properties. Sections VIII and IX then introduce the related Lau effect and Talbot interferometer, respectively; and Section X shows how we combine these to create generalized lens-free Talbot–Lau interferometers, suitable for de Broglie wave interferometry. Since we have been unable to find a treatment of Kirchoff scalar diffraction theory for wave propagation in a medium with inhomogeneous index of refraction, we derive its basic results in an appendix, applied to de Broglie wave propagation in a spatially varying potential. Section XI then applies this result to a general discussion of Fresnel diffraction and the Talbot effect for the case of a de Broglie wave interferometer in the earth's gravity field. Finally, Sections XII–XIV discuss atom interferometry experiments that employ the GTL and Talbot effects.

II. SBE Interferometry

The progenitor form of the GTL solid grating interferometer is the separated beam envelope (SBE) solid grating interferometer, first proposed by Clauser (1989) and shown in Fig. 1a. It has been used extensively by Pritchard's group at MIT (Keith *et al.* 1991), (Schmiedmayer *et al.* 1995), (Chapman *et al.* 1995a), (Ekstrom *et al.* 1995). In it, grating G1 is illuminated by a carefully collimated atomic beam. Grating G1 coherently separates the input beam into separated beams via Fraunhofer diffraction. Two of these separated beams are then redirected by a second grating pair, G2A and G2B, to superpose, interfere, and form a transverse standing wave on the face of a third grating, G3. The standing wave is then masked by G3 to form a moiré pattern, so that a measurement of the flux of transmitted atoms allows detection of the interference.

The SBE configuration has quite remarkable image-forming properties. As a result, the standing wave's visibility is unaffected by direction and magnitude variations of the incident **k** vector (i.e., by coma or chromatic aberration). Unfortunately, the parameter range appropriate to atom interferometry usually does not allow one to fully exploit these properties, as strong collimation of the incident atomic beam is required to fully separate the Fraunhofer orders at G2A,

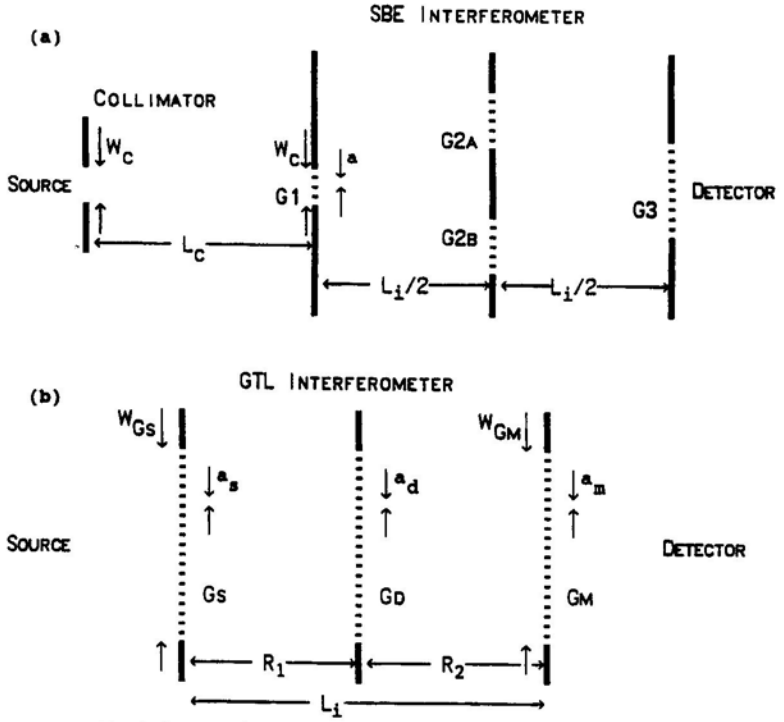

FIG. 1. Layouts for (a) an SBE interferometer, (b) a GTL interferometer.

G2B, and G3. For illumination by a source of atoms with a fixed brightness, B, the transmitted atomic current (in two-dimensions) scales as

$$\text{Current}_{\text{SBE}} \propto B\frac{W_c^2}{L_c} \approx B\left(\frac{\lambda_{dB}}{a}\right)^2 \frac{L_c L_i^2}{(L_i + L_c)^2} \tag{1}$$

where L_c is the collimator length, L_i is the interferometer length, W_c is the collimator width, a is the period of the gratings, and λ_{dB} is the atomic de Broglie wavelength. Unfortunately, for typical available values for λ_{dB} and a, Eq. (1) sets a severe limit to the atomic current transmitted by a SBE interferometer.

III. GTL Interferometry vs. SBE Interferometry

The layout for a GTL interferometer is shown in Fig. 1b. It eliminates the collimator entirely and consists simply of a set of three very wide diffraction gratings Gs, Gd, and Gm, in sequence. (Rather than identifying these gratings as G1, G2,

and G3, as we have in previous works, here we use the notation Gs, Gd, and Gm to indicate their functions as source, diffraction, and mask gratings.) A GTL interferometer's transmitted atomic current correspondingly scales as $BW_{Gs}W_{Gm}/L_i$, where L_i is the interferometer's total length, and W_{Gs} and W_{Gm} are the Gs and Gm grating widths. Since there is no limitation to the widths W_{Gs} and W_{Gm}, then, relative to a SBE interferometer, a GTL interferometer provides an enormously higher throughput atomic current for a given source brightness. For interferometry with slow atoms, where available source brightness is considerably less than that for fast atoms, the increased throughput (ratio of fringe intensity to illuminating source brightness) can be dramatic. For example, in our first GTL atom interferometer (Clauser and Li, 1994a), the source brightness was 2500 times weaker than that of MIT's first SBE interferometer (Keith *et al.*, 1991). Nonetheless, the peak-to-peak transmitted current variation of the interference signal was 3000 times stronger. This throughput improvement (by nearly a factor of 10^7) can be readily extended by another factor of 10^3 through the use of larger gratings and/or gratings with a higher open area fractions.

How does it work? In a GTL interferometer, each point within each slit of Gs acts as an independent source. For each such source, diffraction grating Gd produces strongly overlapped Fraunhofer diffraction orders on the face of Gm. However, in this overlap region, Fresnel diffraction applies and the various orders coherently superpose to create a form of wave interference *unique to Fresnel diffraction,* called the *Talbot effect.* As with SBE interferometry, the interference produces a standing de Broglie wave on the face of Gm, thereby allowing Gm to act as a mask, so that the wave interference may be detected by laterally scanning a grating's position. The finite slit widths of Gs and Gm only slightly wash out the transmitted current's associated fringe variation. Thus, while the gratings still physically separate an atom's interfering paths within the beam's envelope, that envelope itself does not separate. Interfering paths within the envelope consist topologically of many sets of nested diamonds, starting in a given slit on Gs, passing through the various Gd slits, and terminating at a point on Gm, where they interfere.

Now, if Gs is suitably periodic, each Gs slit produces essentially the same standing wave as that produced by other Gs slits. The contributions by all Gs slits then add to the intensity without deteriorating the fringe visibility. This incoherent addition of Talbot fringe patterns is called the *Lau effect.* It is noteworthy that, while the usual demonstrations of the optical Talbot and Lau effects require the presence of one or more lenses, our generalization of these effects allows a lens-free system. Additionally, our GTL configuration retains or even improves on many of the desirable features of SBE interferometry. It has higher grating-misalignment tolerance. Since no collimation is needed, the formation of the standing wave is independent of the source area; hence, no coma occurs. The price paid for the increased angular acceptance, however, is increased chromatic aberration. The standing wave formed at Gm is strongly dependent on illumination wavelength and *is not* a simple geometric shadow effect but a *true* interference effect. Depending on illumination

wavelength, the standing wave period appears at various different harmonics of the shadow period.[1] Actually, this chromatic aberration manifests itself as a resonant chromatic selectivity that proves to be desirable in many instances and can even act as a de Broglie wave interference filter (see Section XV).

There is another dramatic difference between SBE and GTL interferometry. For a given λ_{dB} and interferometer length, GTL interferometry allows grating periods that are at least an order of magnitude larger than those for SBE interferometry. This grating period difference results from different scaling mechanisms for the two schemes. Equation (1) shows that, to maintain a minimum throughput and interferometer size, as the particle mass increases, the SBE grating period must scale directly with $\lambda_{dB} = h/(mv)$. It is noteworthy that MIT's current SBE experiments use microfabricated gratings with a period ($\approx$200 nm) close to the current lower limit for microfabrication. Thus, SBE interferometry with very massive particles seems precluded.

On the other hand, with GTL interferometry, the necessary grating period scales as $\lambda_{dB}^{1/2}$. Figure 2 shows the required Gd grating period, a_d, as a function of

[1]The discussion by Dubetsky and Berman (1994) of the transmission of atoms by three sequential gratings employs only the wavelength independent ($n = 0$, see later) shadow moiré effect, even though their arrangement affords a wide variety of moiré fringe multiplicities, because of the higher spatial frequencies introduced by Gs.

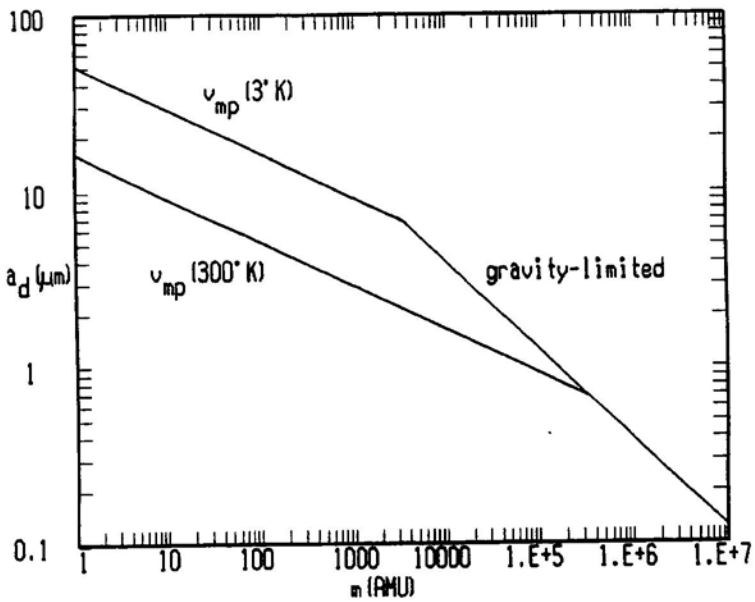

FIG. 2. Required Gd grating period, a_d, as a function of species atomic mass number for a 3 m long $m = 2$ GTL interferometer.

atomic mass number for a 3 m long interferometer. The two lines on the left are for the most probable particle velocity in thermal beams at 300 K and 3 K, respectively, while the right side's limiting line is for freely falling particles gravitationally accelerating in the 3-m interferometer length. The interferometer is assumed here to operate with $a_s = a_m = 2a_d$ at the $n = 1$, $m = 2$ resonance (see later), allowing it to demonstrate wave interference unambiguously. It can be seen that GTL de Broglie wave interferometry with very massive particles such as very large atomic clusters (i.e., very small rocks) or even small live viruses may be achievable in the near future.

IV. What Happens When Fraunhofer Diffraction Orders Overlap?

To appreciate the Talbot effect, it is helpful to understand what happens when Fraunhofer diffraction orders overlap. Consider the simple two-dimensional (2D) Fresnel scalar diffraction pattern formed by the Young's N-slit interferometer depicted in Fig. 3. A point source located at $r_s = (x_s, z_s)$ emits monochromatic waves (classical or quantum mechanical) with wavelength λ. The waves are then passed by a planar finite-extent periodic complex transmitting object (diffraction grating). The grating contains N periods, with period a_d, and is located at $z = z_d$ with $R_1 \equiv z_d - z_s$, with its axis of symmetry located on the z axis. The general solution to this problem will provide the complex amplitude for waves imping-

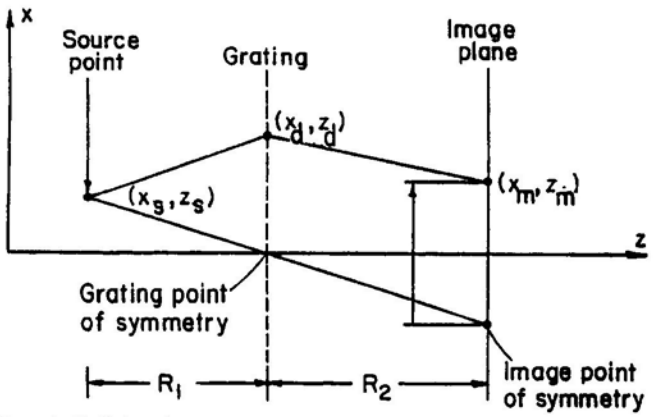

FIG. 3. Young's N-slit interferometer arrangement for demonstrating Fresnel scalar diffraction.

ing on the $z = z_m$ plane, here called the *image plane*, at a point $r_m = (x_m, z_m)$, with $R_2 \equiv z_m - z_d$. Because of complications arising from quadratic phase factors in the Fresnel approximation, this general solution with finite N was delayed until 1992, when it was found by Clauser and Reinsch (1992). A summary of important features of the Clauser and Reinsch (1992) solution is given in Sections VI and VII.

An important distinction between this problem and that for Fraunhofer diffraction is that, in the latter case, plane-wave illumination is assumed, whereupon one must specify $R_1 = \infty$, and then the resulting pattern's scale depends only on the length R_2. In marked contrast, the solution to the present Fresnel problem requires a careful consideration of *both* lengths R_1 and R_2. It is convenient to reparameterize these in terms of two other parameters, the "reduced length," ρ, defined as

$$\rho \equiv \frac{R_1 R_2}{R_1 + R_2} \tag{2}$$

and the geometric shadow magnification, M, defined as

$$M \equiv \frac{R_1 + R_2}{R_1} = 1 + \frac{R_2}{R_1} = \frac{R_2}{\rho}. \tag{3}$$

It will soon become apparent that the quantity

$$\lambda_{TR} \equiv a_d^2/\rho \tag{4}$$

named the *Talbot–Rayleigh wavelength* by Clauser and Reinsch (1992), is also a very important parameter in this problem.

Surprising features emerge from the solution of this simple diffraction problem. These are illustrated by a straightforward numerical evaluation of the Kirchoff diffraction integral, as is done by Clauser and Reinsch (1992) and reprinted here in Figs. 4a–4f. For all of this figure the calculation is for a simple binary grating composed of 12 unit-transmission slits, each of width s_d, with $s_d/a_d = 1/3$, $R_2 = 1$, $a_d = 10^{-6}$, and $\lambda = 5 \times 10^{-8}$—all held constant, thereby freezing the positions of the Fraunhofer diffraction orders to integral multiples of 500×10^{-6}. (If MKS units are assumed, the parameter range spanned will be found to be appropriate for a typical atom interferometer.) Each successive part of the figure represents a situation with the source moved progressively closer to the grating. That is, among these parts, the value of R_1 varies, starting in Fig. 4a at $R_1 = \infty$, taking on progressively decreasing values, and yielding correspondingly increasing values for λ_{TR} and M. Each part displays two graphs. The upper trace shows the image intensity, and the lower trace shows the associated geometric shadow ($\lambda = 0$) image of the grating.

Fraunhofer order overlap does not occur (Clauser and Reinsch, 1992, Section 1.5) as long as the product $N\lambda_{TR}$ is less than the illuminating wave-

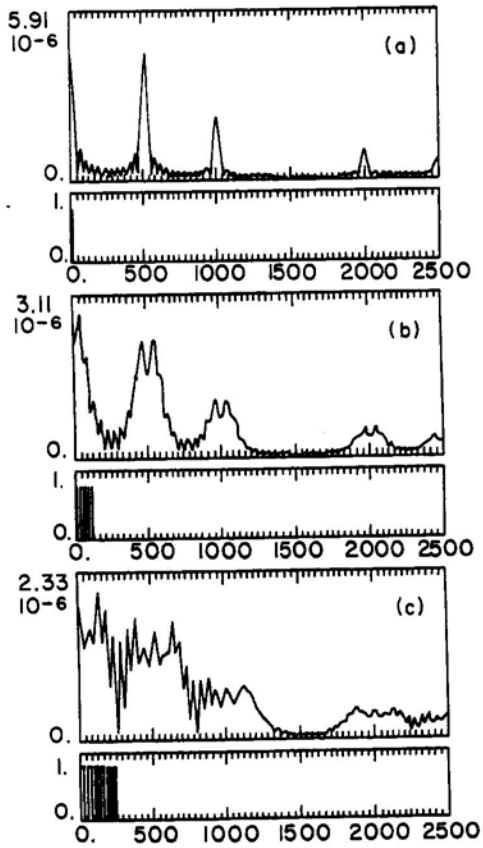

FIG. 4. (a–c) Fresnel diffraction patterns and (d–f) geometric shadow patterns as a function of x_m, for $x_s = 0$ produced by the arrangement of Fig. 3 for various values of R_1 but all with the same fixed λ and R_2. Fraunhofer orders always occur at integer multiples of 500 (see text). Fresnel patterns are normalized correctly only relative to each other, while shadow patterns are renormalized to 1. (Figure adapted from Clauser and Reinsch, 1992.)

length, λ. For the present calculation, R_2 was chosen sufficiently large that $N\lambda_{TR}$ is smaller than λ for both Figs. 4a and 4b. In turn, these two parts display well-formed Fraunhofer diffraction orders. Figure 4c corresponds to $N\lambda_{TR} = \lambda$, where the order structure now resembles a step function. Figures 4d, 4e, and 4f, all correspond to cases with $N\lambda_{TR} > \lambda$. Figures 4d–4f show cases with $N\lambda_{TR} > n\lambda_{TR} = \lambda$, where n ($<N$) is an integer (3, 2, and 1, respectively). Each part shows n equally spaced, non sinusoidal "fringes" formed

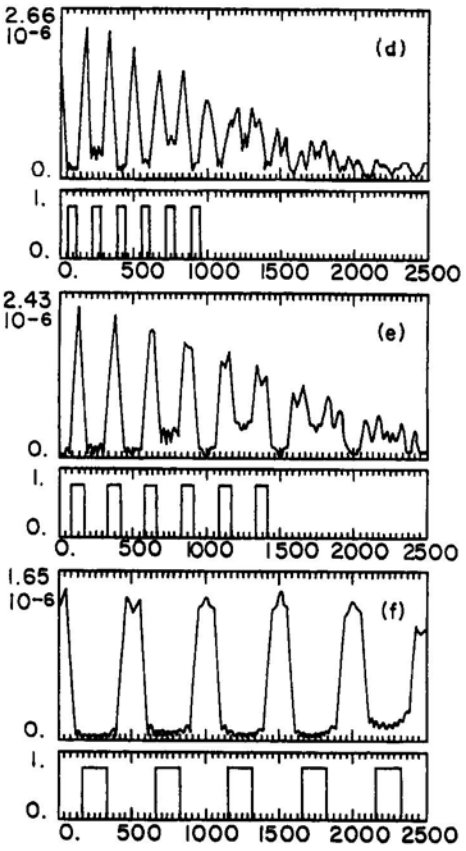

FIG. 4. (continued)

per order separation. When this calculation is performed for a grating with much larger N, the features in Figs. 4d–4f "fringes" become rectangles, with the same shapes (except for Gibbs phenomena) as those of the associated geometric shadows.

The presence of these regular "fringes" in Figs. 4d–4f is *not* self-evident from an inspection of the form of the Kirchoff diffraction integral. Moreover, for intermediate choices for R_1 such that n is not an integer, the pattern displays highly irregular features. The regular features seen here are examples of what we call the *generalized* (finite-N) *Talbot effect*.

V. Historical Development of the Generalized Talbot Effect

A different manifestation of the surprising periodicities evident in Figs. 4d–4f was first noticed experimentally (with light) by Talbot (1836). His apparatus is shown in Fig. 5a. A beam of monochromatic light is focused to parallel by a lens and directed through a coarse periodic binary transmission grating (Ronchi ruling) with large N. In analogy with the arrangement of Fig. 3, his arrangement effectively sets $R_1 = \infty$ and $M = 1$. In contrast to the variation of Fig. 4, it varies λ_{TR} by varying R_2. In addition, a second identical grating is placed in the transmitted light to act as a mask, aligned so that its slits and plane are maintained parallel to those of the first grating. An observation consists of varying the lateral position of either grating while monitoring the transmitted light for different choices for the separation R_2 between the grating planes.

When the spacing between the gratings R_2 is 0 (i.e., when they contact each other), the lateral position variation yields a simple moiré (triangular) variation of the transmitted intensity. When the gratings are slightly separated, diffraction initially blurs the moiré variation. However, at grating spacings, R_2, equal to integral multiples of a characteristic length, the moiré fringes reappear at nearly 100% visibility! The inescapable conclusion is that, with monochromatic light, a

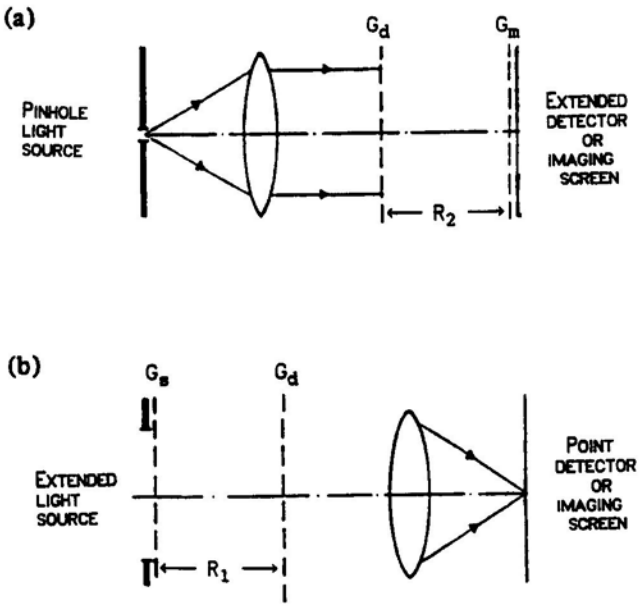

FIG. 5. (a) Talbot's experiment, (b) Lau's experiment.

grating at these spacings can produce a nearly exact image of itself. Furthermore, this self-imaging must intimately involve wave interference, since the characteristic length is wavelength dependent.

Talbot's effect remained totally mysterious until Lord Rayleigh (1881) noted that it is intimately associated with a nonvanishing wavefront curvature and identified the characteristic length in Talbot's experiment. The first detailed explanation of this long-standing mystery was first given in 1957 in the landmark work by Cowley and Moodie (1957). They solved the problem depicted in Fig. 3 for an infinite periodic transmission grating with an arbitrarily shaped (real) single-period transmission function. To do so, they used a Fourier series technique. Self-evident in their resulting formulas is a direct prediction of the self-images observed by Talbot. They named these images *Fourier images*.

In their further experimental observations, however, Cowley and Moodie (1957) found a wide variety of additional, now even more mysterious, shorter-period periodic images.[2] The regularities of these images are *not* self-evident from an inspection of the Cowley and Moodie (1957) formulas.[3] They named these additional mysterious images *Fresnel images*. Rogers (1963) studied Fresnel images numerically, while Hiedemann and Breazeale (1959) presented additional experimental evidence for them. Winthrop and Worthington (1965, 1966) provided a (not particularly transparent) method for calculating Fresnel images by introducing what they called the *Fresnel transform* but provided no transform inversion method.

The first correct classification of Fresnel images was given by Gori (1979; see also, Sudol and Thompson, 1979), working in the domain of binary gratings with "sufficiently narrow" slits. Gori showed that the resulting fringe "multiplicities" (relative to the geometric shadow period) are governed by a ratio of two integers, n and m, in which m controls the fringe multiplicity, while n accounts for the periodic recurrence of the self-images. He also experimentally demonstrated this effect. Additionally, Gori presents a qualitative argument to show that the finite extent of a binary grating limits the allowed multiplicity of the Fresnel images, while Smirnov (1979) gives an order-of-magnitude estimate for their depth of focus. Patorski (1989, 1993) provides reviews of these and other treatments up to 1992.

The problem depicted in Fig. 3 with both finite and infinite periodic complex gratings was first given an exact analytic solution by Clauser and Reinsch

[2]Cowley and Moodie (1957) comment, "In fact it is observed that with gratings of this type a large number of sharp and frequently complicated out-of-focus patterns are generated."

[3]These images may be calculated using the Cowley and Moody (1957) formulas, although Cowley and Moodie did not appear to recognize this fact. Indeed, they comment (Cowley and Moodie, 1957, p. 499) that "No obvious relationship exists between the positions of the delta functions and the maxima and minima of the real and imaginary parts of the Fourier transform of the Fresnel wave function."

(1992). They provide formulas for calculating both the detailed fringe and envelope shape. More important, in the Clauser and Reinsch (1992) formulas the formation of both Fourier and Fresnel images *is* self-evident by inspection. Further, Clauser and Reinsch (1992) show that in the $N \rightarrow \infty$ limit the image *amplitude* of the Fourier images become exact complex amplitude self-images of the grating. With finite gratings, "filtered" amplitude self-imaging occurs instead. Clauser and Reinsch also show that Fresnel images consist of multiply added (aliased) laterally displaced Fourier self-images. In addition, they give a formula for the spatial frequency spectrum of the fringe intensity showing finite-width "resonances" at the integer ratios discovered by Gori. In the finite-N domain, the Clauser and Reinsch (1992) formulas also predict a small spatial frequency shift of the fringe pattern, new effects associated with a detuning from a resonance, limitations to the spatial frequency spectrum set by finite grating extent, and a number theoretical relationship between n and N.

VI. Spatial Properties of the Generalized Talbot Effect "Image"

The Clauser and Reinsch (1992) analysis shows that the basic requirement for a "fringe" resonance to occur, or equivalently for a Fourier or Fresnel "image" to form, is set by Gori's (1979) condition:

$$\frac{\lambda_{\mathrm{TR}}}{\lambda} = \frac{a_d^2}{\lambda \rho} = \frac{m}{n} + \epsilon \tag{5}$$

where m and n are small integers, generalized by Clauser and Reinsch to allow for a tuning error, ϵ. These integers are what we call here *resonance indexes* (quantum numbers). Equation (5) represents a *fundamental constraint* for the generalized (finite-N) Talbot effect to occur.

So-called Fourier fringes are formed on the image plane for $m = 1$ and integer values of $n \geq 1$. The terms *fringe* and *image* may be applied only loosely to the pattern formed on the "image plane," as the pattern's shape, in general, is nonsinusoidal and not an image, either, in the usual sense. Indeed, the pattern's amplitude is a magnified (by M) near replica of the complex grating amplitude transmission function itself. For $N < \infty$, the pattern is a filtered (slightly rounded) amplitude self-image, with the associated filtering given by the Clauser and Reinsch (1992) Eqs. (25)–(27). In the $N \rightarrow \infty$, $\epsilon = 0$ limit, the self-image is an exact magnified replica. For $N < \infty$, the filtered self-image has a finite envelope (produced via Clauser and Reinsch (1992) Eq. (25)) that is comparable to the grating's magnified finite shadow width. For a finite N, approximate self-imaging persists for a finite range of $\epsilon \neq 0$, limited by the inequality, $|\epsilon| < 2/(nN)$, which results from a finite remainder in the integer division of Eq. (5).

It should be noted further that the Clauser and Reinsch (1992) treatment holds exactly *only* when n is a factor (rational divisor) of N, the number of slits. For modestly large N, the Clauser and Reinsch (1992) Eqs. (23)–(27) still yield an approximate but increasingly accurate prediction for the resulting pattern. Recently, Clauser and Dowling (1996) show further that with small slit widths, all such "fringes" will have the same height *if and only if* n is a rational divisor of N. They then use this result to show that the simple Young's N-slit interferometer depicted in Fig. 3 can be used as an analog computer to find the integer factors of N.

So-called Fresnel fringes are formed on the image plane for integer values, $m > 1$ and $n \geq 1$. Clauser and Reinsch (1992) generalize the Gori (1979) and Cowley and Moodie (1957) results to cover general complex gratings, so as to show that the pattern now consists of m copies (aliases) of the "filtered" $m = 1$ (Fourier) amplitude self-image per geometric shadow period, with the associated complex amplitudes all added together. The result is a periodic pattern with period Ma_d/m. Thus, the resonance index m is referred to as the *alias multiplicity.* Because of this addition, the added set of images is no longer a self-image of the original grating, although each of the added components is such a self-image. Correspondingly, for $m > 1$, the summed pattern for a binary grating does not preserve the original grating's slit-width to period-width ratio. Also, when the added components overlap, their added amplitudes interfere, so that the integer fraction m/n is always reduced to its lowest terms.

The $m = 1$ case is obviously consistent with the $m > 1$ case, as the Fourier image case represents the Fresnel image case, where only one copy, the filtered self-image itself, is present. Correspondingly, other features of the $m = 1$ case discussed earlier, also persist in the $m > 1$ case. Finally, it should be noted that, whenever the product $m \times n$ is odd (whether or not N is finite), the whole pattern is shifted laterally (relative to the position of the geometric shadow pattern) by half a shadow (magnified) period.

VII. Wavelength Dependence of the Spatial Spectrum of the Fringe Intensity

Even with small integer values for the resonance indexes, m and n, many possible rational fractions occur, with each such fraction providing a "resonance." The effect of $m > 1$ aliasing will be to introduce (or intensify) the mth harmonic of the basic geometric shadow period into (in) the spatial spectrum of the image intensity. Each of the intensity's various spatial frequency components then contains a regular set of finite-width resonances as a function of the illuminating wavelength, λ. These are shown in Fig. 6. Here we display the λ dependence of the lowest (m-dominated) five Fourier coefficients of the intensity for the limit-

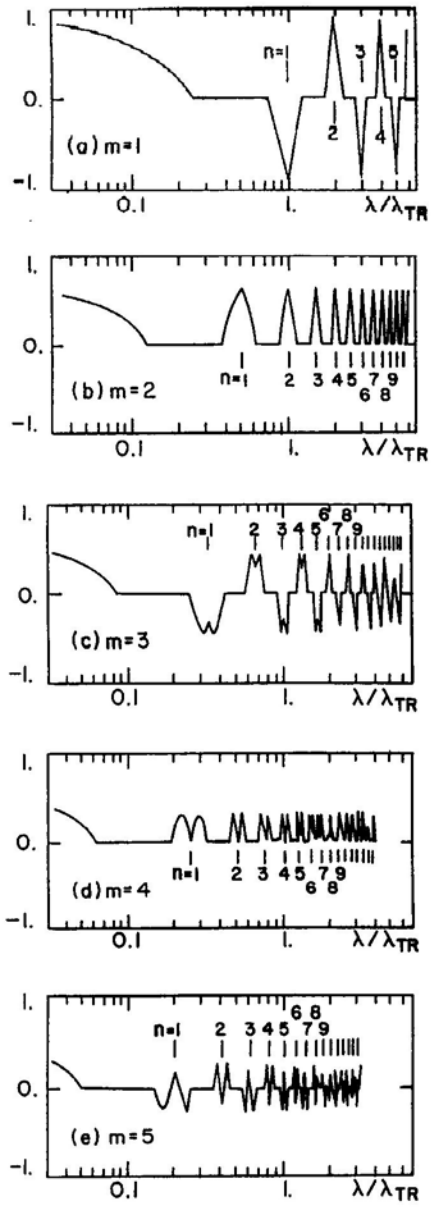

FIG. 6. Wavelength dependence of the $m = 1 - m = 5$ spatial Fourier components of the intensity pattern for a $N = \infty$ binary grating with $\omega/a = 1/4$. (Figure adapted from Clauser and Reinsch, 1992.)

ing case of a binary grating composed of an infinite number ($N = \infty$) of slits, where the intensity has become exactly periodic. Here, the slits have a width, s_d, and period, a_d, with $s_d/a_d = 1/4$. In contrast to the geometric variation employed in Section IV, here the geometry (and λ_{TR}) is held fixed and only the wavelength varies. The Fourier series expansion of the intensity used here has all real coefficients and should not be confused with Cowley and Moodie's Fourier expansion of the image amplitude.

For the important case of a binary grating (used for Fig. 6), each resonance has sharply defined boundaries (Clauser and Reinsch 1992, Eqs. (57) and (59), and the resonance full widths are given by

$$|\epsilon| \leq \frac{m s_d}{n^2 a_d}, \qquad \frac{\Delta\lambda}{\lambda} = \frac{2 s_d}{n a_d}. \tag{6}$$

For modestly high s_d/a_d, the contribution by each multiplicity-m alias is associated dominantly with the associated mth harmonic content. Cases a, c, and e in the figure show odd valued multiplicities, $m = 1$, 3, and 5. Correspondingly, these spectra display negative values for the associated Fourier coefficient when $m \times n$ is odd, as a result of the associated half-period shift of the pattern. Cusps occur in the $m = 4$ resonances shown in Fig. 6d, because, when the wavelength is tuned exactly to a resonance, with $s_d/a_d = 1/4$, four quarter-period slit images add together to produce a flat intensity distribution.

The condition $n = 0$, $\epsilon = 0$, holds when the wavelength λ exactly vanishes; that is, the $\lambda \to 0$ ($n = 0$, $\epsilon \to 0$) limit is the geometric shadow limit. Figure 6 shows that for small but finite λ, the mth Fourier coefficient of the shadow pattern vanishes abruptly at $\lambda/\lambda_{TR} = s_d/(m a_d)$, with the coefficient for the fundamental ($m = 1$) component correspondingly persisting to longest wavelength.

For $N < \infty$, the image is no longer periodic and each Fourier component obtains a finite spectral width, while the number of resonances for each value of m is limited by N and results in image filtering. The $N < \infty$ spatial spectrum is given by the Clauser and Reinsch (1992) Eqs. (57) and (59). We further note that these formulas hold whether or not n is a factor of N. As a result, when multiplied by the Fourier transforms of the Gs and Gm intensity transmissions (suitably adjusted by the "shifting theorem"), they provide the least computationally intensive method for numerically calculating the exact intensity transmission for a GTL interferometer as a function of grating displacement.

VIII. The Lau Effect

Lau (1948) performed an experiment similar to that by Talbot. A diagram of his apparatus is shown in Fig. 5b. In Lau's experiment, a diffuse extended (spatially incoherent) monochromatic source illuminates a wide, coarse binary grating.

The transmitted light then passes through a second identical grating and a lens. A screen is placed at the focal distance of the lens to observe the magnified patterns thus produced. As before, when the grating spacing, R_1, is an integral multiple of Rayleigh's characteristic length, nearly exact images of the gratings are formed on the screen.

One may assume negligible transverse coherence in the narrow bandwidth light illuminating Lau's first grating, Gs. Each point within a slit of Gs then acts as an isolated, independent point source illuminating grating Gd, spaced from Gs by R_1. Each such source point generates a Talbot effect image on the screen. Lau has effectively placed the image at $R_2 = \infty$ by the use of a lens. Incoherently averaging the intensity produced by all such points within a given source grating slit yields the intensity produced by one such slit. Now, since the resulting pattern is periodic, a second Gs slit spaced at a distance $a_s = a_d$ from the first slit will produce the same pattern, simply shifted by one period. Hence, all source slits produce essentially the same periodic image (except for finite envelope-width effects) that is observed on the screen for one slit, and the intensities from all Gs slits add.

IX. The Talbot Interferometer

The next step in understanding the operation of a GTL interferometer is to discuss what is commonly referred to as the *Talbot interferometer*, first demonstrated by Lohmann and Silva (1971). Its configuration is essentially identical to that of Fig. 5a, with an imaging screen acting as the detector (following the second grating). The spacing R_2 is set so that the $m = 1$, $n = 1$ resonance obtains for Gd. In a variant configuration by Yokozeki and Suzuki (1971), a laser replaces the point source and lens. When a refractive object is inserted between the two gratings, a shadow image of the object forms on the screen. Image features depend on the object's refractive index gradient distribution.

X. Generalized Lens-Free Talbot–Lau Interferometers

Given an understanding of the Lau effect, one can see that another interferometer, similar to the Talbot interferometer, may be created by combining the Talbot and Lau effects. This may be done by simply adding a "masking" grating, Gm, to the image plane in Lau's experiment. Equivalently, one can replace Talbot's point source with a diffuse source, followed by a "source" grating Gs. However, neither combination is particularly useful for atom interferometry, since both involve the use of a lens. Indeed, Patorski reviews a variety of experiments using similar arrangements, all involving the inclusion of one or more lenses. Unfortunately, interferometric quality lenses do not, as yet, exist for atom de Broglie waves.

We can see, however, that lenses are readily eliminated from a Talbot–Lau interferometer by suitable choices for the grating periods or for the resonance indexes associated with diffraction by Gd. Thus, a lens-free generalized Talbot–Lau interferometer (Reinsch and Clauser, 1991) suitable for atom de Broglie wave interferometry may be created by simply placing three gratings in sequence and employing spatially incoherent de Broglie wave illumination, as we have done in Fig. 1b.

Consider the simple symmetric ($R_1 = R_2$) example shown in Fig. 1b. If the wavelength, grating spacing, and Gd period, a_d, are chosen so that the $m = 1$, $n = 1$ resonance obtains, then the fringe period formed on Gm by a point source on the Gs plane will be $Ma_d/m = 2a_d$. If the Gs and Gm periods are chosen to be $a_s = a_m = 2a_d$, then the Lau effect will occur and the resulting self-image "fringes" formed on the Gm plane may be detected by moiré techniques, as before, by monitoring the transmission of Gm and its variation under a lateral translation of any one of the three gratings.

It should be noted that a wide variety of choices is possible for grating periodicities, resonance indexes, and associated grating spacings. To obtain highest throughput, gratings with periods $a_s = Ma_d/(mM - m)$ and $a_m = Ma_d/m$ are appropriate. Clauser and Reinsch (1992) experimentally demonstrate operation of a lens-free asymmetric GTL interferometer for light operating at the $m = 3$, $n = 1$ resonance that employs illumination by a spatially incoherent sodium discharge lamp. Another useful variant is with $R_1 = R_2$, $m = 2$, and $a_s = a_d = a_m$. This latter case, however, will not allow one experimentally to distinguish $m = 1$ and $m = 2$ resonances from each other.

A gravity gradiometer (Clauser, 1988, 1989, 1991), (Marzlin and Audrecht, 1995) may be built using a GTL interferometer composed of four gratings, shown in Figs. 7a and 7c. Here, Gs and Gd separated by R_1 (T_1) create a periodic "real" image at an image plane a distance R_2 (T_2) behind Gd. Rather than placing a masking Gm grating at this plane, this image acts as a periodic source for a second Gd′ diffraction grating placed $R_1' = R_2$ behind Gd. A final masking Gm grating placed $R_2' = R_1$ behind Gd′ then detects the fringes.

Finally, it should be noted that, since self-images are amplitude images, one may use a phase grating for Gd. Indeed, Janike and Wilkens (1994) use a standing wave laser beam to act as an atom de Broglie wave phase grating in an arrangement useful for high-resolution lithography. One may also consider the possibility of observing a "temporal" Talbot effect, where laser phase gratings are sequentially pulsed so that the atomic velocities multiplied by the time intervals yield appropriate values for R_1 and R_2 (see Section XI). Analyzed in this regard, however, it will be seen that the experiment by Mossberg *et al.* (1979) operates in the $n = 0$ geometric shadow regime.*

*See endnote, p. 150.

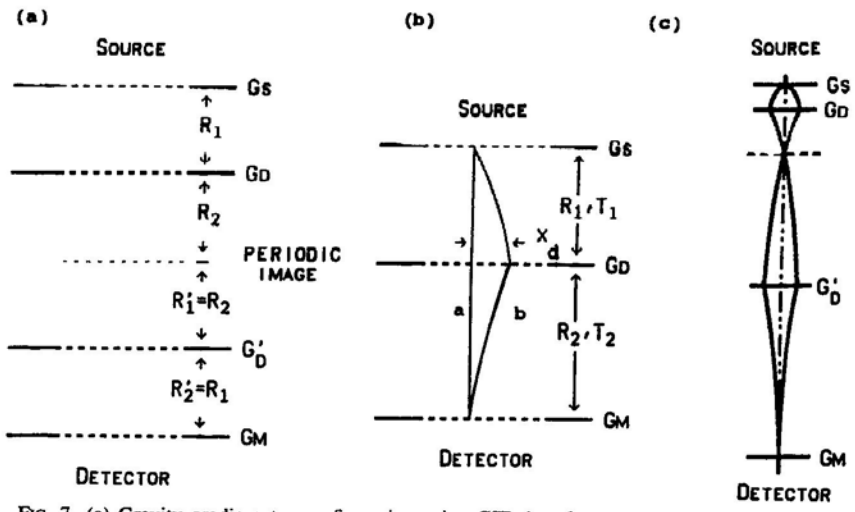

FIG. 7. (a) Gravity gradiometer configuration using GTL interferometry and four gratings. (b) Vertical GTL interferometer in a gravitational field. (c) Gravity gradiometer configuration of (a) with R_1 and R_2 having equal fall times, also showing typical (patented) figure 8 interfering paths within the beam's envelope.

XI. Fresnel Diffraction and the Talbot Effect with a Spatially Varying Potential

So far, we have discussed Fresnel diffraction and the Talbot effect for de Broglie wave propagation under a constant potential, $V(\mathbf{r}) = V$. In such case we have $k \equiv |\mathbf{k}(\mathbf{r})| = 2m[E - V]^{1/2}/\hbar, \equiv 2\pi/\lambda_{dB}$ and the path integral (see the appendix) is just simply $k|\mathbf{r} - \mathbf{r}'|$. However, we noted in Section IX that a detectable fringe shift will result if, at any place between the gratings of a Talbot interferometer, a change in the intervening index of refraction occurs. For de Broglie waves the index of refraction is given by $n(\mathbf{r}) = [1 - V(\mathbf{r})/E]^{1/2}$ and will be spatially varying in the presence of nonvanishing Coriolis, gravitational, electric, and/or magnetic fields. The appendix presents a derivation of the Kirchoff diffraction integral for de Broglie wave diffraction in the presence of a slowly spatially varying (with respect to λ_{dB}) potential $V(\mathbf{r})$. Here, we apply the results of this appendix to demonstrate how the Talbot effect still occurs and how the associated fringe shifts may be evaluated for a few simple cases.

When $V(\mathbf{r}) \ll E$ is not constant, a simple approximation may be used to evaluate the path integrals (Anadan, 1984), (Greenberger and Overhauser, 1979). The approximation is to neglect the path curvature, which is now small, and perform the path integration along a straight-line path, which is not far from the desired classical path Γ_{cl}. Moreover, if the variation of $V(\mathbf{r})$ is

uniform through the propagation volume, as is the case when $V(\mathbf{r})$ is due to gravity, it will contribute a common error to all paths that will cancel. The use of exactly horizontal or vertical gratings significantly improves the accuracy of this approximation. For the case of fast particles in a gravitational field, when the trajectory is roughly horizontal, this approximation yields a simple classical fall of the envelope and the fringes at the image plane for both SBE and GTL interferometers.[4]

With very slow atoms (and long λ_{dB}), unless one somehow eliminates the pull of the earth's gravity, then the potential energy, $V(\mathbf{r}) = mgz\hat{\mathbf{e}}_z$, is not small with respect to E and the associated classical path curvature may not be neglected, even in an interferometer with exactly horizontal gratings. Consider a particle falling from a point $\mathbf{r}_1 = (x = 0,\ z = 0)$ to a point $\mathbf{r}_2 = (x = x_2,\ z = -L)$. The path integral, via Eq. (A6), is then given by

$$\Phi(\mathbf{r}_1,\mathbf{r}_2) = \frac{2mg^{1/2}}{3\hbar}\left[2\ell + L + \frac{1}{2}(4L\ell + 4\ell^2 - x_2^2)^{1/2}\right]$$
$$\times \{[L + 2\ell + (L^2 + x_2^2)^{1/2} - [L + 2\ell - (L^2 + x_2^2)^{1/2}]^{1/2}\} \tag{7}$$

where $\ell \equiv E/(mg)$.

We now apply Eq. (7) to a vertical axis interferometer with horizontal gratings operating in the earth's gravity field, as shown in Fig. 7b. We calculate the phase difference between two representative paths, a straight down reference path and one passing through a Gd slit a distance x_d off the axis. To apply the Fresnel approximation, we express Eq. (7) as a power series in x_d, keeping terms only to the second order. Terms of higher order are negligible for $x_d^2 \ll 4\ell R_1$. The phase difference is then given by

$$\frac{\Phi_b - \Phi_a}{2\pi} \approx \frac{mx_d^2}{2h}\left(\frac{1}{T_1} + \frac{1}{T_2}\right). \tag{8}$$

Here, T_1 and T_2 are the fall times for a classical particle through the associated distances R_1 and R_2. A comparison of the form of Eq. (8) with that for the $V = 0$ case (Clauser and Reinsch 1992, Eq. (4)), $\Delta\phi/(2\pi) = x_d^2/(2\lambda\rho)$, provides the definition

$$(\lambda_{dB}\rho)_{eff} \equiv \frac{h}{m}\frac{T_1T_2}{T_1 + T_2}. \tag{9}$$

which, in turn, may be used in place of Eq. (2) to allow a direct application of the Clauser and Reinsch (1992) formulas for GTL interferometry in terms of the classical fall times in place of axial vertical fall distances. Equation (7) may be used in similar fashion to evaluate higher order phase shifts, aberrations, the ef-

[4]Note, however, that in a (two–loop) gravity gradiometer the envelope falls but the fringes do not.

fects of grating period foreshortening associated with a path's oblique incidence on a grating, and so forth, for an arbitrarily inclined interferometer in the earth's gravity field.

XII. GTL Atom Interferometry Experiments with K and Li_2

The first working GTL atom interferometer was demonstrated by us at the University of California—Berkeley (UCB) (Clauser and Li, 1994a). The experimental arrangement is shown in Fig. 8. The atomic beam source actually gener-

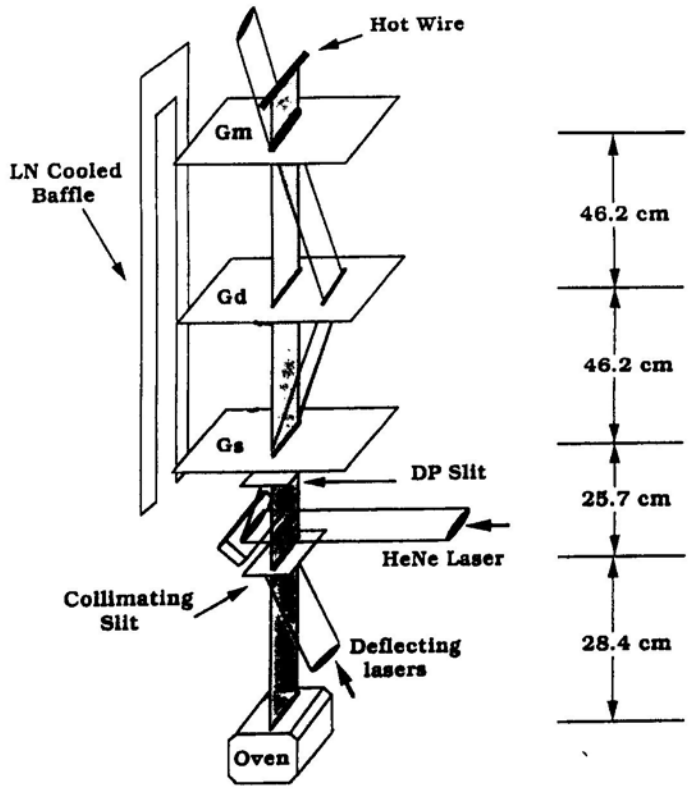

FIG. 8. Generalized Talbot–Lau atom interferometer used by Clauser and Li (1994a). Grating rotational alignment uses a HeNe laser that forms a SBE optical interferometer using all three atom gratings and a fourth additional identical grating, displaced to one side of Gd. (Figure adapted from Clauser and Li, 1994a.)

ates two copropagating atomic beams: a dc hot thermal beam and an ac-modulated cold slow potassium beam. Thermal potassium atoms effuse from an oven, pass through a wide collimating slit (needed for velocity selection only), and then through an atom de Broglie wave GTL interferometer to a hot wire (surface ionization) detector. The oven slit is offset from the interferometer axis so that only one wing of the collimated thermal beam (produced by scattering near the oven slit) passes through the interferometer to the detector. Cold slow atoms are velocity selected by using laser light to deflect them out of the offset parent thermal beam onto the interferometer axis (Li and Clauser, 1994). The laser beam crosses the atomic beam immediately below the collimating slit at 20° from comoving parallel. The parallel component of the laser's propagation vector provides Doppler velocity selection of atoms from the low-velocity portion of the parent beam's thermal distribution, while the perpendicular component provides momentum transfer for deflection. The small deflection angle (≈.5 mrad.) requires scattering of only about seven photons, so that perpendicular heating of the slow atoms is minimal and a source brightness of about 4×10^{15} atoms cm^{-2} sr^{-1} sec^{-1} is achieved for 182 m/sec atoms.

The ac modulation of the deflecting laser allows the transmission of the two different beam components to be measured independently. The average dc hot wire signal represents that due to the thermal velocity component of the atomic current. The weak ac component of the current is synchronously detected by an "up/down boxcar integrator." The maximum transmitted ac current is roughly 4×10^5 atoms per sec at 182 m/sec. The dc current is about 130 times stronger, and the signal to noise ratio of the AC signal is limited by the shot noise of the much larger copropagating dc current.

The interferometer consists of a sequence of three microfabricated rectangular vacuum-slit transmission gratings. The gratings are microfabricated from 1 μm-thick silicon nitride membranes supported by silicon frames, with parallel slits etched through the membranes. Grating fabrication was done by us at UCB's Microfabrication Lab via conventional optical lithography and etching techniques. The interferometer's parameters are $R_1 = R_2 = 46.2$ cm, $a_s = a_m = 16.2$ μm, $a_d = 8.1$ μm, $N_s = 22$, $N_d = 111$, and $N_m = 76$ slits. All gratings are 8.5 mm long with $\lambda/a \approx 1/8$. Fringes are sensed by measuring the interferometer's transmission as a function of Gd position. The fringe pattern and transmitted current contain various spatial harmonics of the geometric shadow period, with each harmonic resonant in the interferometer at a different atomic velocity (different λ_{dB}). The hot beam produces a pattern that appears as diffraction-limited shadow moiré fringes, shown in Fig. 9a. Its high spatial frequency Talbot fringe structure is washed out by the thermal velocity average. (In Section XIV, we show how components of this structure may be recovered and observed.) The ac-modulated slow beam produces high-visibility interference fringes at the 5th and 6th spatial harmonics of the shadow moiré, via excitation of the $(m,n) = (5,1)$, and $(6,1)$ interferometer resonances, evi-

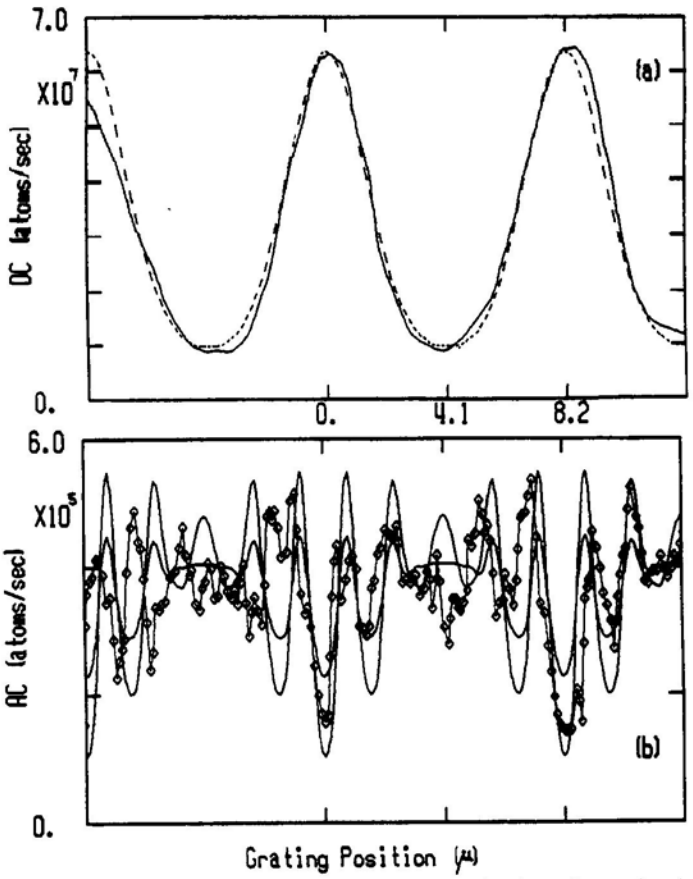

FIG. 9. (a) Diffraction-limited shadow moiré fringes formed with thermal potassium beam illumination of the interferometer of Fig. 8. (b) High-visibility de Broglie wave interference fringes at the 5'th and 6'th spatial harmonics of the shadow period, formed with illumination by a slow cold potassium beam. (Figure adapted from Clauser and Li, 1994a.)

dent in the ac signal, shown in Fig. 9b, and in agreement with numerical simulations.

In these experiments, we also observed that a strong Sagnac phase shift of the pA dc (fast atom) fringe signal was immediately ($t_{\text{int}} < 1$ mS) evident whenever the chamber was touched, even lightly. Using the straight-line path integral approximation of Section XI, we find that this translates to a sensitivity to rotations of $\Omega_{2\pi} \approx 7 \times 10^{-3}$ rad/sec, as the rotation rate needed to provide a 2π phase shift. For the ac (slow atom) sixth harmonic fringes, rotations at $\Omega_{2\pi} \approx 4 \times 10^{-4}$

rad/sec (at a count rate of almost 10^6 atoms/sec) caused similar fringe shifts. For comparison purposes, the atom interferometry experiment by Riehle *et al.* (1991) yielded $\Omega_{2\pi} \approx 0.4$, the neutron interferometer Sagnac effect measurement by Werner *et al.* (1979) yielded $\Omega_{2\pi} \approx 3 \times 10^{-5}$ and the electron interferometer Sagnac effect measurement by Hasselbach and Nicklaus (1993) yielded $\Omega_{2\pi} \approx 46$. Subsequently, we have used the same apparatus (after some modification) to observe fringes from thermal Li_2 molecules. Inserting electric field gradient electrodes, we have used our apparatus to determine the electric polarizability of Li_2.

XIII. Talbot Interferometer Using Na

An example of a de Broglie wave Talbot interferometer (Section IX) was demonstrated using sodium by Chapman *et al.* (1995b). A diagram of their apparatus is shown in Fig. 10a. There is no Gs, since this is not a GTL configuration.

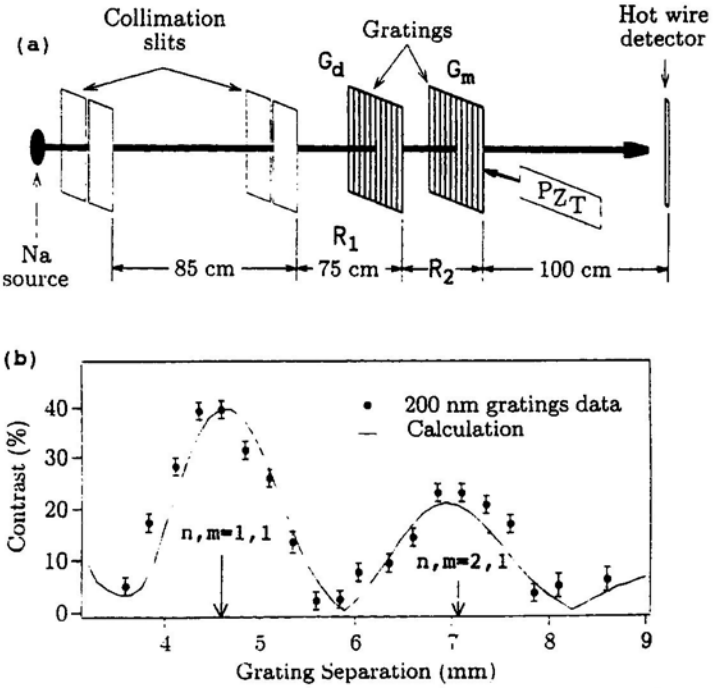

FIG. 10 (a) Talbot interferometer apparatus used by Chapman *et al.* (1995b) (b) Observed fringe "visibility" as a function of R_2, showing the $n = 1$, $m = 1$ and $n = 2$, $m = 1$ resonances. (Figures adapted from Chapman *et al.*, 1995b.)

Instead, they produce a quasi-parallel atomic beam by configuring $R_1 \gg R_2$. The resulting low throughput is compensated for, using brute force, by employing a very bright fast-atom source. Their experiment was performed as a near parallel to Talbot's experiment. By varying the spacing R_2 between the gratings, they observed both the $n = 1, m = 1$ and $n = 2, m = 1$ resonances. Figure 10b shows the observed fringe "visibility" as a function of R_2. The visibility of higher n self-images is reduced by a combination of finite collimator size, lack of exact beam parallelism (equivalently, $M \neq 1$), and finite atomic velocity spread.

XIV. "Heisenberg Microscope" Decoherence GTL Atom Interferometry

Walls *et al.* (1991; see also Tan and Walls, 1993) and, independently, Sleator *et al.* (1992) have analyzed a problem, analogous to that of the "Heisenberg microscope" *gedanken* experiment for freely propagating atoms with well-defined momenta that form de Broglie wave fringes in a Young's two-slit interferometer. They consider a situation where both slits are simultaneously illuminated by a single photon that is resonant with an atomic transition and calculate the resulting atomic fringe visibility as a function of slit separation. They predict that, when the slits are separated sufficiently that a Heisenberg microscope viewing the fluorescent reemission of the photon could image this light to determine which slit an atom passes, the atomic fringe visibility will vanish. But, when the slit spacing is comparable to the optical wavelength, such a determination by the microscope exceeds its resolving power, and then the atomic interference pattern will persist.

While performing the GTL atom interferometry experiment of Section XIII, we recognized that our interferometer could be modified simply to allow testing this prediction in the limit of large slit spacing. While a similar effect had been earlier observed by Sterr *et al.* (1992) with high-intensity scattered light, we were the first to demonstrate (Clauser *et al.* , 1993a–c; Clauser and Li, 1994b) that the scattering of a single low energy photon by an atom passing through an N-slit interferometer with wide slit spacing, $a_d \gg \lambda_{\text{photon}}$, will totally destroy the de Broglie wave interference fringes formed.

To do this, we reconfigured our experiment to that of Fig. 11. For this experiment, we passed *only* a thermal velocity distribution of potassium atoms through the GTL atom interferometer. It produced a thermal velocity average of different fringe Fourier components, with each component resonant in the interferometer at a different atomic velocity. As noted previously, the velocity distribution averages and hides the high-frequency fringe components. To recover a specific component, we pass very weak ac-modulated laser light diagonally through the interferometer near the middle grating to scatter off of the transiting atoms. Since

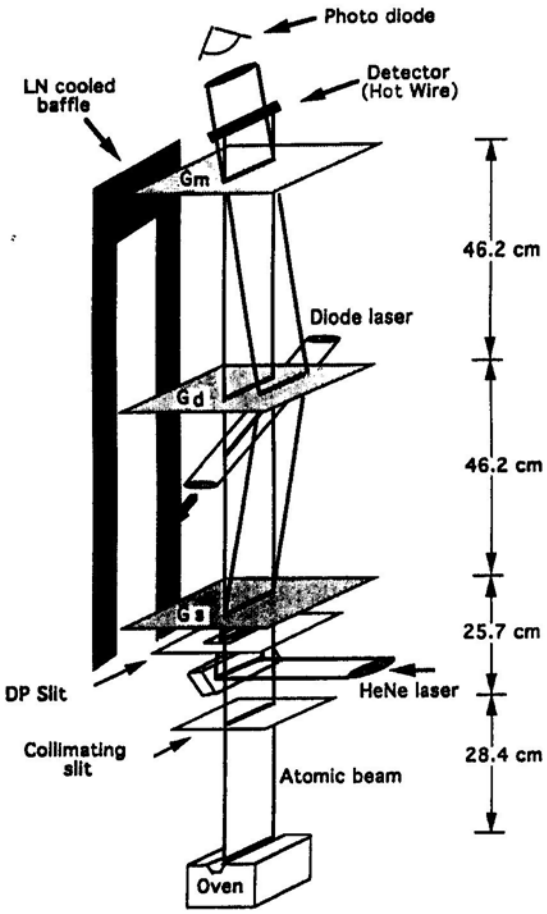

FIG. 11. "Heisenberg microscope" decoherence GTL atom interferometry apparatus used by Clauser and Li (1994b). (Figure adapted from Clauser and Li, 1994b.)

imaging of the scattered fluorescent light *could* be used to determine which slit an atom passes, the scattering removes the contribution to the averaged pattern by atoms whose velocity corresponds to the laser's Doppler-shifted wavelength. That velocity component (only) thus is ac modulated and detected. Its ac modulation then reveals the destroyed high spatial-frequency fringe contribution. Thus, to observe the destroyed fringe pattern, we record the ac transmitted atom current as a function of Gd position, while holding the laser tuning fixed. The results are shown in Fig. 12.

When the laser is on, photons are scattered by the atoms. Given our GTL

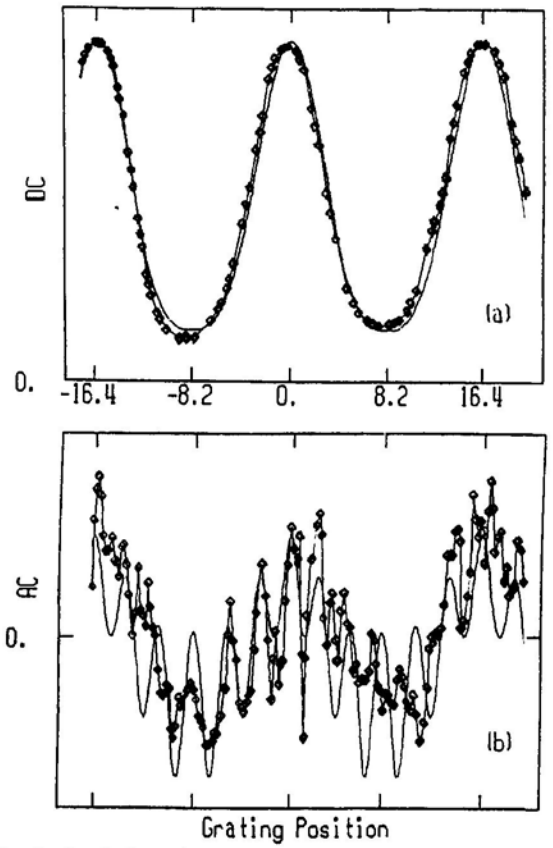

FIG. 12. (a) The dc signal (thermal beam transmission) recorded for the arrangement of Fig. 11 as a function of Gd lateral position. (b) The associated ac signal for constant laser tuning displaying the interference fringe pattern destroyed by the scattering of a single photon. (Figure adapted from Clauser and Li, 1994b.)

geometry and sufficient momentum transfer from the photon, atoms may be scattered into open slits and thence transmitted. We model this process assuming a classical atomic trajectory and use the pointwise momentum-transfer photon scattering model developed by Einstein in his discussion of the kinematics required for thermal equilibrium to be produced when a gas is irradiated by thermal light. The potassium hyperfine structure effectively limits the number of photons scattered by an atom to about one via the high probability that following a scattering the atom will optically be pumped and thereafter be transparent to

the laser radiation. To further assure less than one photon's scattering per atom in an atom's flight time through the laser beam, and to provide a narrow effective laser bandwidth, the laser is attenuated heavily.

To test this model, we measure the velocity (laser-tuning) dependence of the ac signal while holding the grating positions fixed. While the hyperfine structure is not resolved in the fluorescence spectrum, by contrast, the ac transmission spectrum displays two well-resolved peaks whose spacing corresponds to the hyperfine structure. In effect, we thus have used the chromatic selectivity of a GTL interferometer to create here what amounts to an atom interference filter. The filter's velocity selectivity has allowed us to narrow the effective transmitted velocity range, to provide an improvement in the optical fluorescence spectral resolution.

Subsequently, Pfau *et al.* (1994) have further improved on our experiment by measuring the coherence loss as a function of slit spacing. Pfau's group is now pursuing a third generation experiment in which the scattered photon is detected in coincidence with the scattered atom.

XV. Conclusions and Future Applications

The fringe deflection at the final masking grating produced by a weak external field, such as that resulting from gravitational and Coriolis forces, is the classical deflection in either a SBE or GTL interferometer. Hence, for comparable masking of grating slit widths and comparable atomic velocities, the fringe shifts due to these forces (or any other weak deflecting force) are identical. However, for comparable source brightness, the transmitted atomic current in a GTL interferometer is many orders of magnitude higher than that of a SBE interferometer. In addition, the brightness afforded by most sources for very slow atoms generally is too weak to be used in SBE interferometers. Hence, GTL interferometry offers much higher sensitivity than SBE interferometry for the measurement of weak deflecting forces, in view of its potential for dramatically superior signal to noise ratio.

The study of GTL interferometry also is a source of new physics. Figure 2 shows that GTL interferometry may be applied to species with very large mass and thereby can probe the fundamental limits for a possible breakdown of de Broglie wave interference as the classical domain is approached. As the study of the quantum mechanics of large atoms and molecules advanced beyond considerations of the hydrogen atom, it yielded new surprises and new quantum numbers. In a direct parallel, extending one's consideration of Young's two-slit configuration to that of the N-slit configuration has revealed new surprises in diffraction theory, including new quantum numbers (m and n), a rich new spectroscopy (see Fig. 6), a surprising relationship between number theory and dif-

fraction theory, and possible new insights for quantum computing (Clauser and Dowling, 1996).

Presently in progress in our laboratory is an experiment to observe de Broglie wave interference with freely falling very cold Rb atoms. Using now standard techniques to provide a bright source, the atoms are dropped from a MOT (see Shimizu *et al.*, 1992) and focused with a magnetic lens (see Cornell *et al.*, 1991) through a GTL interferometer. This configuration is particularly interesting for study, since the atoms experience a form of gravitational pseudo-cooling during their fall (sometimes referred to as *dynamic velocity compression*), so that the velocity distribution incident on Gd (as viewed in the lab frame) is much narrower than that of the MOT.

Appendix: Kirchoff Diffraction with Spatially Varying $V(\mathbf{r})$

Unlike a light-pulse interferometer, a grating interferometer is an inherently static device. Thus the wave function, $\psi(\mathbf{r})$, of a particle with energy E propagating through such a device in the presence of a static potential $V(\mathbf{r})$ must satisfy the time-independent Schrödinger equation, which may be written in the form of the Helmholtz equation as

$$[\nabla_r^2 + k^2(\mathbf{r})]\psi(\mathbf{r}) = 0 \tag{A1}$$

with $k_2(\mathbf{r}) = 2m[E - V(\mathbf{r})]/\hbar^2$. Since the Helmholtz equation is the time-independent parent equation for propagation of many other types of waves, our discussion applies to these cases as well. In turn, the Green's function, $G(\mathbf{r}; \mathbf{r}')$ for this problem satisfies the equation

$$[\nabla_r^2 + k^2(\mathbf{r})]G(\mathbf{r}; \mathbf{r}') = \delta(\mathbf{r} - \mathbf{r}'). \tag{A2}$$

The diffraction problem to be solved involves the boundary conditions of Fig. 3. Consider a trial Green's function:

$$G(\mathbf{r},\mathbf{r}') = \frac{e^{i\phi(\mathbf{r};\mathbf{r}')}}{|\mathbf{r}-\mathbf{r}'|}. \tag{A3}$$

Substituting Eq. (A3) into Eq. (A2), we find that the phase function, $\phi(\mathbf{r}; \mathbf{r}')$, satisfies the equation

$$\left\{k^2(\mathbf{r}) - \left[\nabla_r\phi(\mathbf{r}; \mathbf{r}')\right]^2\right\} + i\left[\nabla_r^2 - \frac{(\mathbf{r} - \mathbf{r}')}{|\mathbf{r} - \mathbf{r}'|^2}\cdot\nabla_r\right]\phi(\mathbf{r}; \mathbf{r}') = 0. \tag{A4}$$

For a slow spatial variation of $V(\mathbf{r})$ (with respect to λ_{dB}) such that the WKB approximation holds, that is, such that $|\nabla,\phi|^2 \gg |\nabla_r^2\phi|$ holds, and outside of the "very near-field" region such that $|\nabla\phi| \gg 1/|\mathbf{r} - \mathbf{r}'|$ holds, then Eq. (A4) becomes

$$|\nabla_r\phi(\mathbf{r}; \mathbf{r}')|^2 \approx k^2(\mathbf{r}) = 2m[E - V(\mathbf{r})]/\hbar^2. \tag{A5}$$

Without a loss of generality, we take $\phi(\mathbf{r};\,\mathbf{r}) = 0$. Then, given the identity $\phi(\mathbf{r}_2;\,\mathbf{r}_1) = \int_{\mathbf{r}_1}^{\mathbf{r}_2} \nabla\phi(\mathbf{r};\,\mathbf{r}_1)\cdot d\mathbf{r}$ for any integration path, we see that $|\phi(\mathbf{r}_2;\,\mathbf{r}_1)|$ must be no greater than the extremum among possible integration paths, Γ, of the *path-dependent* line integral $\int_{\mathbf{r}_1;\Gamma}^{\mathbf{r}_2} |\nabla\phi(\mathbf{r};\,\mathbf{r}_1)|\, dl(\mathbf{r})$. This extremum occurs for the path that is always locally tangent to $\nabla_{\mathbf{r}}\phi(\mathbf{r};\,\mathbf{r}_1)$; that is, for the path for which $|\nabla\phi(\mathbf{r};\,\mathbf{r}_1)\cdot d\mathbf{r}| = |\nabla\phi(\mathbf{r};\,\mathbf{r}_1)|\, dl(\mathbf{r})$ holds throughout. However, a classical particle with energy E traveling from $\mathbf{r}_1$ to $\mathbf{r}_2$ under the influence of $V(\mathbf{r})$ will have its momentum $\mathbf{p}_{cl}(\mathbf{r}) = m\mathbf{v}_{cl}(\mathbf{r})$ always tangent to its trajectory, Γ_{cl}, with $|\mathbf{p}_{cl}(\mathbf{r})|^2 = 2m\,[E - V(\mathbf{r})]$. The path Γ_{cl} may be found by solving Hamilton's equations for the classical motion. By Eq. (A5), we then have $|\mathbf{p}_{cl}(\mathbf{r})|^2 = \hbar^2 |\nabla_{\mathbf{r}}\phi(\mathbf{r};\,\mathbf{r}')|^2$, and from *Maupertuis's principle of least action*, we know that the path Γ_{cl} is the desired extremum integration path. Therefore, the solution to Eq. (A5) is given by the path integral

$$\hbar\phi(\mathbf{r}_2;\,\mathbf{r}_1) = \pm\int_{\mathbf{r}_1;\Gamma_{cl}}^{\mathbf{r}_2} \mathbf{p}_{cl}(\mathbf{r})\cdot d\mathbf{r} = \pm\int_{\mathbf{r}_1;\Gamma_{cl}}^{\mathbf{r}_2} \sqrt{2m[E - V(\mathbf{r})]}\, dl(\mathbf{r}). \tag{A6}$$

Given our trial Green's function of Eqs. (A3) and (A6), we may write the amplitude transmitted by the grating of Fig. 3 with amplitude transmission $t(\mathbf{r}_d)$ at any point $\mathbf{r}_d$ on the $z = z_d$ plane, in response to a point source at $\mathbf{r}_s$, as

$$\psi(\mathbf{r}_d) = \frac{e^{i\phi_r(\mathbf{r}_d;\mathbf{r}_s)}}{|\mathbf{r}_d - \mathbf{r}_s|}\, t(\mathbf{r}_d)\psi(\mathbf{r}_s). \tag{A7}$$

For the solution to the right of the grating for the problem of Fig. 3, we construct a Green's function satisfying the Rayleigh–Sommerfeld boundary conditions, using instead $[\delta(\mathbf{r} - \mathbf{r}') + \delta(\mathbf{r} - \mathbf{r}'')]/2$ for the right-hand side of Eq. (A2), where we have defined $\mathbf{r}'' \equiv \mathbf{r}' - 2\,(z - z_d)\hat{\mathbf{e}}_z$, and take the limit as $\mathbf{r}' \to \mathbf{r}''$. It is given by

$$G(\mathbf{r},\mathbf{r}') = \frac{e^{i\phi(\mathbf{r};\mathbf{r}')}}{|\mathbf{r} - \mathbf{r}'|} \pm \frac{e^{i\phi(\mathbf{r};\mathbf{r}'')}}{|\mathbf{r} - \mathbf{r}''|}. \tag{A8}$$

Via Green's theorem, the amplitude at any point $\mathbf{r}_m$ on the $z = z_m$ image plane is given by the integral over the $z = z_d$ surface S as

$$\psi(\mathbf{r}_m) \approx i\psi(\mathbf{r}_s) \times \int_S \frac{e^{i[\phi(\mathbf{r}_s;\mathbf{r}_d) - \phi(\mathbf{r}_d;\mathbf{r}_m)]}}{|\mathbf{r}_s - \mathbf{r}_d|\;|\mathbf{r}_d - \mathbf{r}_m|}\, \hat{\mathbf{e}}_z\cdot\mathbf{p}_{cl}(\mathbf{r}_d)t(\mathbf{r}_d)\, da(\mathbf{r}_d) \tag{A9}$$

where $da(\mathbf{r}_d)$ is a differential area on S.

We note a formal resemblance between the Green's function $G(\mathbf{r}_1;\,\mathbf{r}_2)$ and the Feynmann propagator $K(\mathbf{r}_1,t_1;\,\mathbf{r}_2,t_2)$. The latter is used by Storey and Cohen-Tannoudji (1994) in their application of Feynmann path-integral methods to atom interferometers. While their method is more appropriate for time-dependent problems (such as light-pulse interferometers), ours is more suitable for time-in-

dependent problems. Both methods evaluate the final amplitude by an integration over all possible classical path contributions to the final amplitude. Both methods evaluate the phase shift along a "classical" path from $\mathbf{r}_1$ to $\mathbf{r}_2$ and integrate over a variation of an endpoint for this classical motion, thereby specifying a family of integration paths. *However, the classical physics assumed for the motions along these paths is quite different, as are the paths within each family.* In our family (that for the Kirchoff diffraction integral), the classical paths Γ_{cl} are all for a particle with a constant energy E but with a varying propagation time; while in a Feynmann path integral family, they are all for a particle with a fixed propagation time $t_2 - t_1$ but with a varying total energy E.

Acknowledgments

This work was supported by the Office of Naval Research and the firm J. F. Clauser & Assoc., Walnut Creek, CA.

Endnote

After completion of this manuscript, an example of the "temporal" Talbot effect predicted herein was experimentally demonstrated by Weitz *et al.* (1996). Effectively, in their experiment 5-slit multipath de Broglie wave interference is created in momentum space via a sum of quadratic phase factors, wherein the interfering paths form nested diamonds. The "slits" are magnetic sublevels of a cesium atom excited by a sequence of three "walking-wave" light pulses, equally spaced in time. Nonsinusoidal interference fringes are observed in the fluorescence as a function of optical phase-shift.

References

Altshuler, S. and Frantz, L. M. (1973). U.S. Patent 3,761,721.

Anadan, J. (1984). *Phys. Rev. D* **30**, 1615.

Chapman, M. S., Ekstrom, C., Hammond, T., Rubenstein, R., Schmiedmayer, J., Wehinger, S., and Pritchard, D. (1995a). *Phys. Rev. Lett.* **74**, 4783.

Chapman, M. S., Ekstrom, C. R., Hammond, T. D., Schmiedmayer, J., Tannian, B. E., Wehinger, S., and Pritchard, D. E. (1995b). *Phys. Rev.* **A51**, R14.

Chebotayev, V. P., Dubetsky, B. Ya., Kasantsev, A. P., and Yakovlev, V. P. (1985). *J. Opt. Soc. Am. B: Opt. Phys. B* **2**, 1791.

Clauser, J. F. (1988). *Physica B* **151**, 262.

Clauser, J. F. (1989). U.S. Patent 4,874,942.

Clauser, J. F. (1991). U.S. Patent 4,992,656.

Clauser, J. F., and Reinsch, M. W. (1992). *Appl. Phys. B* **54**, 380.

Clauser, J. F, Reinsch, M. W., and Li, S. (1993a). *Bull. Am. Phys. Soc.* **38**, 1135.

Clauser, J. F, Reinsch, M. W., and Li, S. (1993b). *Bull. Am. Phys. Soc.* **38**, 1762.

Clauser, J. F, Reinsch, M. W., and Li, S. (1993c). *Optical Society of America Technical Digest* **16**, 215.

Clauser, J. F., and Li, S. (1994a). *Phys. Rev. A* **49,** R2213.
Clauser, J. F., and Li, S. (1994b). *Phys. Rev. A* **50,** 2430.
Clauser, J. F., and Dowling, J. P. (1996). "*Phys. Rev. A* **53,** 4587.
Cornell, E., Monroe, C., and Wieman, C. (1991). *Phys. Rev. Lett.* **67,** 2431.
Cowley, J. M., and Moodie, A. F. (1957). *Proc. Phys. Soc. B* **70,** 486, 497, 499, and 505.
Dubetsky, B. Ya., and Berman, P. R. (1994). *Phys. Rev. A* **50,** 4057.
Dubetsky, B. Ya., Kazantsev, A. P., Chebotaev, V. P., and Yakovlev, V. P. (1984). *Pis'ma, Zh. Eksp. Teor. Fix.* **39**(11), 531.
Ekstrom, C. R., Schmiedmayer, J., Chapman, M. S., Hammond, T. D., and Pritchard, D. E. (1995). *Phys. Rev. A* **51,** 3883.
Gori, F. (1979). *Opt. Commun.* **31,** 4.
Greenberger, D. M., and Overhauser, A. W. (1979). *Rev. Mod. Phys.* **51,** 43.
Hasselbach, F., and Nicklaus, M. (1993). *Phys. Rev. A* **48,** 143.
Hiedemann, E. A., and Breazeale, M. A. (1959). *J. Opt. Soc. Am.* **372,** 372.
Janike, U., and Wilkens, M. (1994). *J. Phys. II Fr.* **4,** 1975.
Keith, D. W., Ekstrom, C. R., Turchette, Q. A., and Pritchard, D. E. (1991). *Phys. Rev. Lett.* **66,** 2693.
Lau, E. (1948). *Ann. Phys.* **6,** 417.
Li, S., and Clauser, J. F. (1994). *Phys. Rev. A* **49,** 2702.
Lohmann, A. W., and Silva, D. E. (1971). *Opt. Commun.* **2,** 423.
Marzlin, K. P., and Audrecht, J. (1995). "State Independence in Atom Interferometry and Insensitivity to Acceleration and Rotation." Konstanz Univ. Preprint KONS-RGKU-95-05.
Mossberg, T., Kachru, R. K., Whittaker, E., and Hartmann, S. R. (1979). *Phys. Rev. Lett.* **43,** 851.
Patorski, K. (1989). *In* "Progress in Optics XXVII" (E. Wolf, ed.), p. 1. Elsevier, Amsterdam.
Patorski, K. (1993). "Handbook of the Moiré Fringe Technique." Elsevier, Amsterdam.
Pfau, T., Spalter, S., Kurstsiefer, C., Ekstrom, C. R., and Mlynek, J. (1994). *Phys. Rev. Lett.* **73,** 1223.
Lord Rayleigh (1881). *Philos. Mag.* **11,** 196.
Reinsch, M. W., and Clauser, J. F. (1991). *Bull. Am. Phys. Soc.* **36,** 1312.
Riehle, F., Kisters, T., Witte, A., Helmcke, J., and Bordé, C. (1991). *Phys. Rev. Lett.* **67,** 177.
Rogers, G. L. (1963). *Br. J. Appl. Phys.* **14,** 657.
Schmiedmayer, J., Chapman, M. S., Ekstrom, C. R., Hammond. T. D., Wehinger, S., and Pritchard, D. E. (1995). *Phys. Rev. Lett.* **74,** 1043.
Shimizu, F., Shimizu, K., and Takuma, H. (1992). *Phys. Rev. A* **46,** R17.
Sleator, T., Carnal, O., Pfau, T., Faulstich, A., Takuma, H., and Mlynek, J. (1992). *In* "Proceedings of the Tenth International Conference on Laser Spectroscopy" (M. Ducloy *et al.*, eds.), p. 264. World Scientific, Singapore.
Smirnov, A. P. (1979). *Opt. Spectrosc.* **46,** 319.
Sterr, U., Sengstock, K., Müller, J. H., Bettermann, D., and Ertmer, W. (1992). *Appl. Phys. Lett. B* **54,** 341.
Storey, P., and Cohen-Tannoudji, C. (1994). *J. Phys. II* **4,** 1999.
Sudol, R., and Thompson, B. J. (1979). *Opt. Commun.* **31,** 105.
Talbot, H. (1836). *Philos. Mag.* **9,** 401.
Tan, S. M., and Walls, D. F. (1993). *Phys. Rev. A* **47,** 4663.
Walls, D. F., Tan, S., Storey, P., and Collett, M. (1991). *In* "Foundations of Quantum Mechanics" (T. Black, *et al.*, eds.), p. 157. World Scientific, Singapore.
Weitz, M., Heupel, T., and Hänsch, T. W. (1996). *Phys. Rev. Lett.* **77,** 2356.
Werner, S. A., Staudenmann, J.-L. and Colella, R. (1979). *Phys. Rev. Lett.* **42,** 1103.
Winthrop, J. T., and Worthington, C. R. (1965). *J. Opt. Soc. Am.* **55,** 373.
Winthrop, J. T., and Worthington, C. R. (1966). *J. Opt. Soc. Am.* **56,** 588.
Yokozeki, S., and Suzuki, T. (1971). *Appl. Opt.* **10,** 1575 and 1690.